



Type of the Paper (Communication)

Laser diffraction zones and spots from three-dimensional graded photonic super-crystals and moiré photonic crystals

Noah Hurley 1, Steve Kamau 1, Khadijah Alnasser 1, Usha Philipose 1, Jingbiao Cui 1, and Yuankun Lin 1,2,*

- ¹Department of Physics, Univ. of North Texas, Denton, TX 76203, USA; noahhurley@my.unt.edu (N.H.); SteveKamau@my.unt.edu (S.K.); KhadijahAlnasser@my.unt.edu (K.A.); usha.philipose@unt.edu (U.P.); Iing-biao.Cui@unt.edu (J.C.)
- ² Department of Electrical Engineering, Univ. of North Texas, Denton, TX 76203, USA.
- * Correspondence: yuankun.lin@unt.edu; Tel.: +1-940-565-4548

Abstract: The laser diffraction from periodic structures usually shows isolated and sharp point-pattern at zeroth and ±nth orders. Diffraction from 2D graded photonic super-crystals (GPSCs) has demonstrated over 1000 spots due to the fractional diffractions. Here, we report the holographic fabrication of three types of 3D GPSCs through nine beam interference and their characteristic diffraction patterns. The diffraction spots due to the fractional orders are merged into large-area diffraction zones for these three types of GPSCs. Three distinguishable diffraction patterns have been observed: (a) 3×3 diffraction zones for GPSCs with a weak gradient in the unit super-cell; (b) 5×5 non-uniform diffraction zones for GPSCs with a strong modulation in a long-period and a strong gradient in the unit super-cell; (c) more than 5×5 uniform diffraction zones for GPSCs with a medium gradient in unit super-cell and a medium modulation in the long-period. The GPSCs with a strong modulation appear as moiré photonic crystals. The diffraction zone-pattern not only demonstrates a characterization method for the fabricated 3D GPSCs but also proves their unique optical properties of the coupling of light from zones with 360° azimuthal angles and broad zenith angles.

Keywords: graded photonic crystals; interference lithography; diffraction

1. Introduction

Traditional Photonic crystals (PhCs) are nano/micro-structures where the dielectric constant is periodically modulated on a length scale comparable to the operation wavelength [1]. There are many applications for two-dimensional (2D) and three-dimensional (3D) PhCs. One of big driving forces for PhC research is its potential for integrated photonics where laser source, single photon emitter, waveguide, filter, coupler, etc. can be integrated [2–6]. For applications in photovoltaic devices, PhCs can be used to enhance the photon absorption within silicon or perovskite solar cells and dye-sensitized solar cells to achieve a high power-conversion efficiency [7–12]. PhCs can also be applied to improve the light extraction efficiency of organic light emitting diode if patterned with the PhC [13–17].

Multiple-beam interference lithography has been used for the fabrication of two-dimensional (2D) and three-dimensional (3D) photonic crystals in large area or volume [18–22]. GPSCs can be fabricated by interfering two sets of beams with different cone angles [23–28], and the optical properties of these graded PhCs will be further studied as they belong to a new group of twisted photonic crystals[29–33], which is a subject still in it's infancy.

Here, we report a holographic fabrication of 3D GPSCs through one central beam and eight side beams where 4 beams symmetrically arranged in cone geometry with a small cone angle α and other 4 beams with a big cone angle β . Three types of dual-period

Citation: Lastname, F.; Lastname, F.; Lastname, F. Title. *Photonics* **2022**, *9*, x. https://doi.org/10.3390/xxxxx

Received: date Accepted: date Published: date

Publisher's Note: MDPI stays neutral with regard to jurisdictional claims in published maps and institutional affiliations.



Copyright: © 2022 by the authors. Submitted for possible open access publication under the terms and conditions of the Creative Commons Attribution (CC BY) license (https://creativecommons.org/license s/by/4.0/).

GPSCs are fabricated with a weak, medium, and strong modulation in the long period. Diffraction patterns are used for non-destructive characterization of quality and distinguishable features of the 3D GPSC.

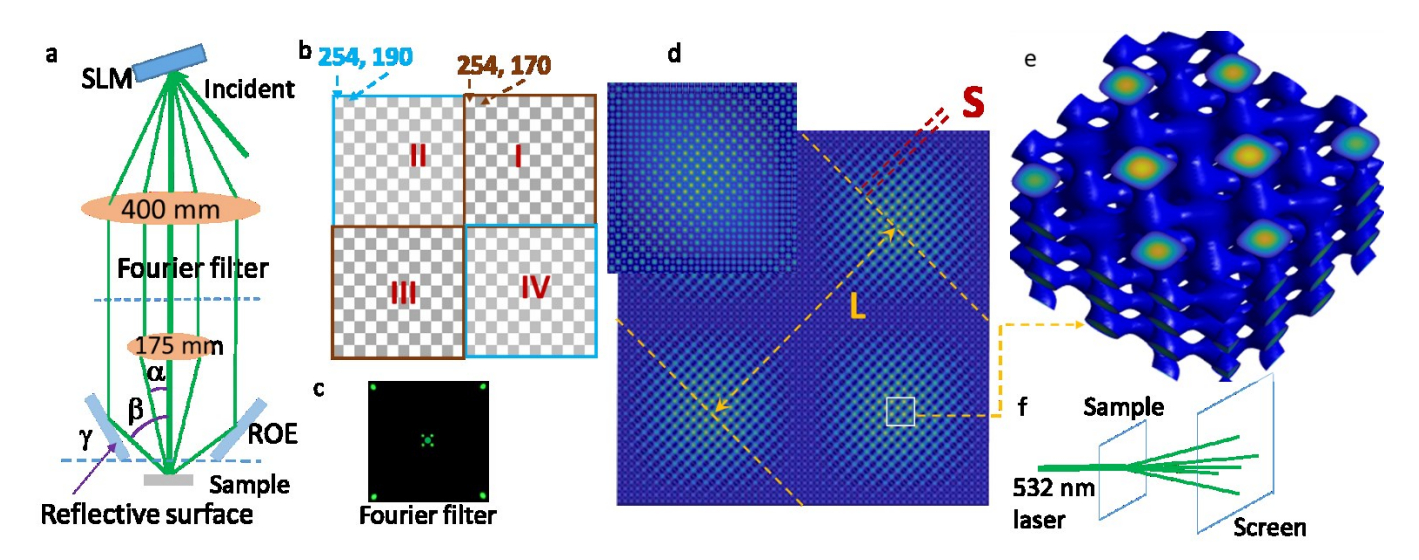


Fig. 1. (a) Schematic diagram of the experimental setup where incident light is diffracted by spatial light modulator (SLM), central and inner beams are imaged through 4f imaging system (f₁=400 mm and f₂=175 mm) and outer beams are reflected by the single reflective optical element (ROE). (b) A design unit of phase patterns in SLM is divided into 4 quadrants and gray levels of 254, 190 are arranged in checkerboard format in quadrant II and IV, and gray levels of 254, 170 are arranged in checkerboard format in quadrant I and III. (c) One central, four inner and four outer beams pass through the Fourier filter. (d) Simulated interference pattern of nine beams assuming a simplified phase shift among the interfering beams. Inset is the interference pattern with a different phase shift among beams. (e) An enlarged view of 3D interference pattern in an area indicated by the solid square in (d). (f) Schematic of diffraction measurement setup for three types of samples.

2. Experimental methods and theoretic description

Figure 1(a) shows the experimental setup for the holographic fabrication. A 532 nm laser (total power: 50 mW, from Cobolt Samba) is incident onto a spatial light modulator (SLM) (Holoeye Pluto phase-only SLM) and linearly polarized along the long side of the SLM. The pixel size of the SLM is 8×8 μm² and we assign one gray level to each pixel. These colored pixels are arranged in a unit of phase pattern as displayed in Fig. 1(b) which covers all 1920×1080 pixels on the SLM. As shown in Fig. 1(b), a design unit of phase patterns in the SLM is divided into 4 quadrants. The gray level of 254 is combined with 190 in a checkerboard format to cover a 12-pixel×12-pixel in quadrant II and IV, and gray levels of 254, 170 are also similarly arranged in checkerboard format in quadrant I and III. One central, four inner and four outer beams pass through the Fourier filter as shown in Fig. 1(c) As shown in Fig. 1(a), the central and four inner beams from SLM are collected by a 4f-imaging system with f₁=400 mm and f₂=175 mm. Four outer beams are collected by the first lens and reflected by single reflective optical element (ROE) printed by our 3D printer. The ROE has four polished silicon wafer pieces, coated with copper by thermal deposition, as the four reflective surfaces. All nine beams are overlapped at the sample.

The intensity of the n-beam interference, I(r), is determined by Eq. (1):

$$I(r) = \langle \sum_{i=1}^{n} E_i^2(r,t) \rangle + \sum_{i < j}^{n} E_i E_j \hat{e}_i \cdot \hat{e}_j \cos[(k_j - k_i) \cdot r + (\delta_j - \delta_i)]$$

$$\tag{1}$$

where E, e. k, δ , are the electric field amplitude, the electric field polarization direction, the wave vector, and the initial phase, respectively. For an accurate simulation of the interference pattern from multiple beams generated from the SLM, each beam needs to be assigned, pixel-by-pixel, the intensity based on the diffraction efficiency [34], and the initial phase based on the gray level [35]. Fig. 1(d) shows a simplified interference pattern

without considering the intensity and initial pixel-by-pixel phase. An enlarged view is shown in Fig. 1(e) for woodpile-like structures, when the phase is changed from π to 0.25π for some beams, the interference pattern shows dot-like structure in inset of Fig. 1(d) instead of the woodpile-like structure.

In the simplified model, the interference pattern can have dual-periods in xy-plane where the small period and large period are indicated by S and L in Fig. 1(d), respectively and can be approximately estimated. The small period is approximately determined by the inferring angle β between central beam and outer beams in Fig. 1(a) by Eq. (2)

$$S = \frac{\lambda}{\sin(\beta)} = \frac{0.532}{\sin(\beta)} \text{ microns}$$
 (2) 89

S=1.93 microns and the interference angle β =180-2 γ with the tilt angle (γ =82 degrees) of the reflective surface in Fig. 1(a). The large period L is approximately determined by the 4f imaging system in Fig. 1(a) and the unit cell size in Fig. 1(b). The diffraction angle θ in Fig. 1(a) for the inner beams is determined by the unit cell size in x-direction which is 24 pixels in Fig. 1(b) by Eq. (3)

24 pixels × sin (
$$\theta$$
) = λ (3) 95

The interference angle α between the central beam and the inner beams is calculated by Eq. (4):

$$\tan \alpha = f_1 \tan \theta \times \frac{\sqrt{2}}{f_2} \tag{4}$$

Considering $tan(\theta) \simeq sin(\theta)$ for a small angle and length of 24 pixels=24×8=192 microns, f₁=400 mm and f₂=175 mm, the large period L in the formed interference pattern in Fig. 1(d) can be approximately calculated by Eq. (5):

$$L = \frac{\lambda}{\sin\alpha} = \frac{192}{\sqrt{2}} \frac{175}{400} = 59.4 \text{ microns}$$
 (5) 102

Three types of holographic structures were fabricated in dipentaerythritol hexapentaacrylate (DPHPA) mixture with a weight percentage as follows: DPHPA monomer (88.88%), a photo initiator rose bengal (0.12%), co-initiator N-phenyl glycine (NPG, 0.8%), N-vinyl pyrrolidinone (NVP, 10.2%). The modified DPHPA mixture was typically spin-coated on glass slides at 2000 RPM for 30 seconds, and exposed to the interference pattern with a typical exposure time between 0.4 and 0.8 seconds. The exposed samples were developed in propylene glycol monomethyl ether acetate for 15 minutes and then allowed to air dry. The diffraction pattern was measured for three types of sample with a setup as shown in Fig. 1(f).

3. Results

3.1. Diffraction zone pattern from holographic structures fabricated with type-1 phase pattern ((254, 190), (254, 170))

We initially used type-1 phase pattern ((254, 190), (254, 170)) in Fig. 1(b) for the imaging system alignment. We present the diffraction pattern from an over-exposed sample, then from a well-developed GPSC. The over-exposed sample has a unique diffraction pattern that can be used to characterize 3D GPSCs. Fig. 2(a) shows a scanning electronic microscope (SEM) of an over-exposed type-1 3D GPSC generated using the type-1 phase pattern ((254, 190), (254, 170)) in Fig. 1(b). There is a weak Fresnel pattern as indicated by dashed circles in the sample in Fig. 2 due to the use of Fourier filter in Fig. 1(c). The weak Fresnel pattern is often used for the alignment of ROE in Fig. 1(a). Figs. 2(b) and 2(c) are the enlarged view of SEMs for the sample in (a) which allow for a clear to see sample that is over-exposed. Along the dashed yellow line in Fig. 2(c), the air filling fraction becomes smaller, which shows the graded nature of the PhCs. The diffraction pattern from the

over-exposed sample is shown in Fig. 2(d) with a 0^{th} order diffraction zone instead of diffraction spot and four weak 1^{st} order diffraction zones. These yellow and blue circles in the figure are for eye-guidance and are located following the 4-fold symmetry of GPSC and the Fresnel pattern in the sample. The edge of these diffraction zones can be fitted by these dashed yellow and blue circles periodically in $[\pm 1 \pm 1]$, $[\pm 1 \ 0]$ and $[0 \pm 1]$ directions. The number of diffraction zones are determined by the long-range order of the modulated GPSC, and the diffraction spots within the diffraction zone are due to the gradient structure in the unit super-cell.

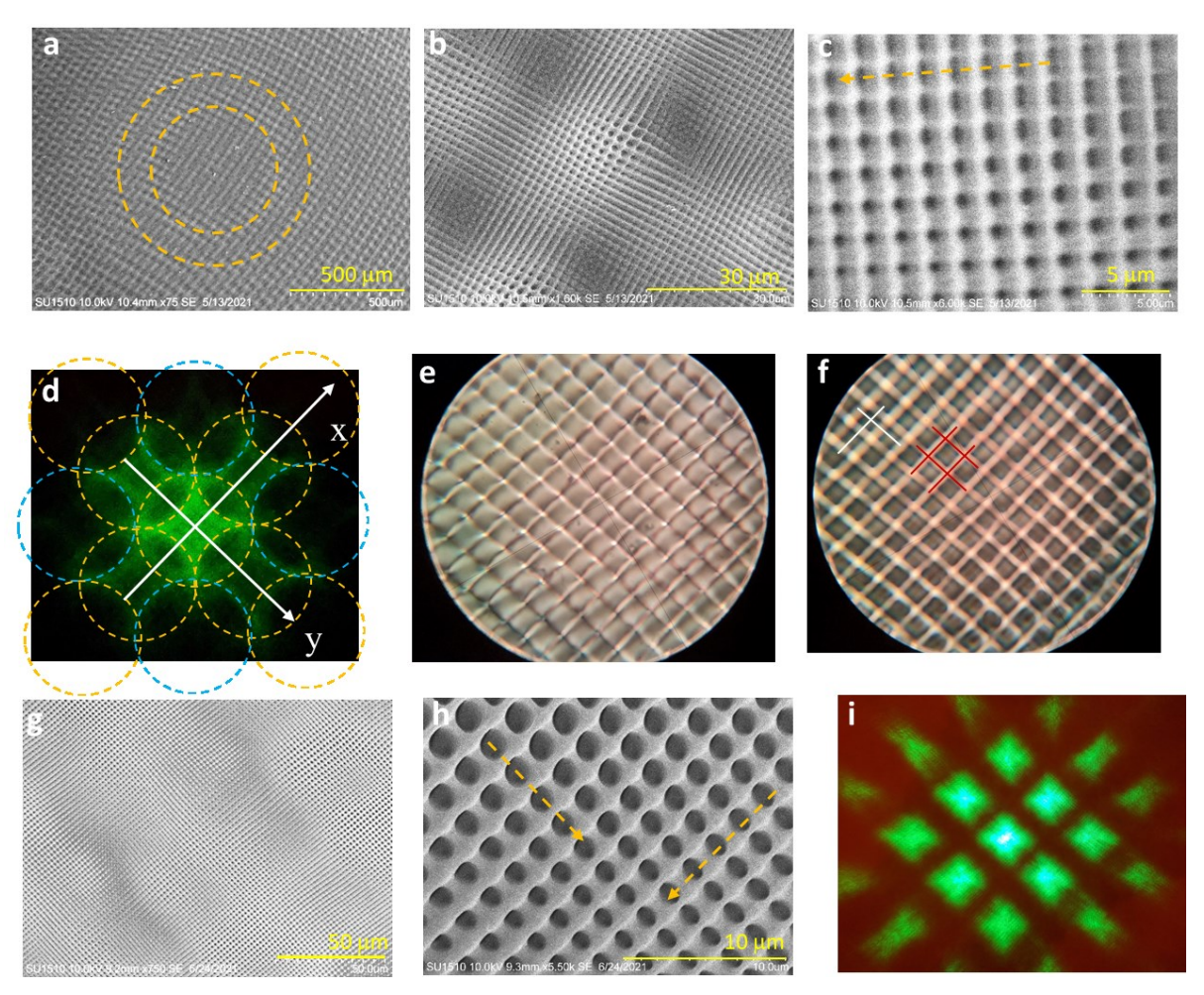


Fig. 2. (a) SEM image of type-1 over-exposed sample with the dashed yellow circles for the eye-guidance of Fresnel pattern, and its enlarged view in (b) and (c). (d) A diffraction pattern from the sample in (a) showing 0th order and 1st order diffraction zones. (e-f) Optical images displaying Talbot diffraction pattern near and farther away from the sample, respectively. (g) SEM image of well-developed type-1 GPSC and its enlarged view in (h). (i) diffraction pattern of well-developed GPSC with 3×3 diffraction zones.

Fig. 2(e) and 2(f) show Talbot diffraction patterns [36] from the overexposed type-1 sample as observed by the optical microscope with the objective lens close to and farther away from the sample, respectively. These patterns and orientations can be understood from the 0th order and four 1st order diffractions in [±1 ±1] directions. In the top half side of Fig. 2(f), the Talbot diffraction pattern looks like a woodpile structure with solid red lines for first and orthogonal second layer patterns while the white lines for the third and fourth layer patterns. Below the woodpile structure, a vague Fresnel pattern appears. These Talbot patterns demonstrate all periodic features in the over-exposed sample.

Fig. 2(g) shows SEM of a well-developed GPSC using the type-1 phase pattern ((254, 190), (254, 170)). The SEM shows that the fabricated GPSC is in a same structure except a variation in height due to the liquid DPHPA mixture. Fig. 2(h) shows an enlarged view of

151

152

153

154

155

156157158

Figure 3. (a) Unit super-cell of type-2 phase pattern with gray levels of (128, 254) in checkerboard format in quadrant I and (128, 2) in quadrant II. (b-c) Enlarged view of checkerboard unit-cell in quadrant I and II, respectively. The phases of diffracted beams are labeled individually. (d) SEM image of type-2 3D GPSC with the solid blue square indicating a unit cell and the dashed yellow line showing the long period of dual-period GPSC, and (e) its SEM image of bottom surface with the dual lattice feature indicated by the white and yellow lines. (f) 5x5 diffraction zones from type-2 3D GPSC. The dashed white square indicates one diffraction zone. (g) the wave vectors for outer beam (blue arrow), inner beam (red arrow) and for central beam (yellow arrow). The dashed red line is slightly tilted from the vertical direction.

3.2. Diffraction zone pattern from holographic structures fabricated with type-2 phase pattern ((128, 2), (128, 254))

The gray levels of (128, 2) and (128, 254) are chosen for type-2 phase pattern because of their high diffraction efficiency from the checkerboard phase pattern in SLM [25,34]. The gray levels of (128, 254) cover quadrant I in Fig. 3(a) in the checkerboard format as shown in Fig. 3(b), while (128, 254) cover quadrant II in Fig. 3(a) in the checkerboard format in Fig. 3(c). These phase patterns modulate the phase of outer diffracted beams through pixel-by-pixel gray levels inside the green dashed square in Fig. 3(b-c) using an equation: phase=0.25*gray level*2 π /255 [35]. The gray level of 254, 128 and 2 generates approximately a phase of π /2, π /4, 0π , respectively, in the diffracted beams. In Fig. 3(b), the phase of the outer beams in [1,1] direction is π /4 higher than these in [1,-1] direction

166

167

168

169

170

171

172

173

174

175

while they are $\pi/4$ less in [1,1] than those in the [1,-1] direction in Fig. 3(c). These phase differences in interfering beams will result in two different patterns, which is observed in Fig. 3(d) where the solid blue square indicates the unit super-cell of fabricated GSPC in DPHPA. Four regions at the vertices of the solid blue square are like the interference pattern in the inset of Fig. 1(d) with the phase shift of 0.25π . The patterns in the center of the solid blue square are similar to the woodpile-like structures in Fig. 1(d-e). The dashed yellow arrow indicates the long period of dual-period GPSC. This GPSC appears also as moiré PhCs. The long period L (also moiré period in this case) is measured to be 58.6 microns, comparing with the theoretically calculated value of 59.4 microns. Fig. 3(e) shows SEM of bottom surface of the sample when it is separated from the substrate after a longer development time than usual one. The moiré pattern is barely able to be seen at the bottom of the surface. The dual lattice feature can be observed [26,34], as indicated by the white and yellow lines. It will be compared with a simulation in next section.

Fig. 3(f) shows the diffraction pattern of the 532 nm laser from the 3D GPSC in Fig. 3(d). The diffraction pattern shows almost 5×5 non-uniform diffraction zones. The dashed white square indicates the size of one diffraction zone. It can be divided into 4 sub-zones corresponding to 4-fold symmetry in the unit super-cell in Fig. 3(d). The edges of the diffraction zone inside the white square in Fig. 3(f) have a parabolic shape, due to the tilt of unit super-cell in 3D GPSC. It can be explained by a simple model in Fig. 3(g). The short period and long period of 3D GPSC in xy-plane are approximately determined by β and α , respectively, in Fig. 3(g). By adding these four inner beams in the interference, the 3D GPSC can be considered to be tilted from vertical direction to the one indicated by dashed red line in Fig. 3(g). Overall, the diffraction zone is not uniform in intensity as indicated by the dashed red lines in Fig. 3(f) for the position of some intensity peaks. The diffraction zones are aligned in diagonal direction as indicated by the dashed yellow (straight or parabolic) lines due to the tilting.

3.3. Diffraction zone pattern from holographic structures fabricated with type-3 phase pattern ((128, 2), (254, 128))

The type-3 phase pattern in the SLM is modified from type-2 in Fig. 3(a). The checkerboard of (128, 254) in quadrants I and III are still the same. The gray levels in the checkerboard quadrants II and IV are switched from (128, 2) to (2, 128). In such a way of arrangement of gray levels, the phase of diffracted beam in Fig. 3(b-c) is changed from $(0.25\pi, 0.5\pi, 0.25\pi, 0.5\pi)$ & $(0.25\pi, 0.5\pi, 0.25\pi, 0.5\pi)$ & $(0.25\pi, 0.5\pi, 0.25\pi, 0.5\pi)$ & $(0\pi, 0.25\pi, 0\pi, 0.25\pi)$ (from top-left along clock wise) for type-3 phase pattern. It means the relative phase shift for diffracted beams from top-left to top-right (also bottom-left to bottom-right) is same for type-3 phase pattern. Although the overall gray levels among quadrants (I, III) and (II, IV) are different for the generation of inner beams, the modulation of the unit super-cell in type-3 3D GPSC is expected to be weaker than that in type-2.

Fig. 4(a-b) shows SEM fabricated 3D GPSC in DPHPA using type-3 phase pattern and its enlarged view. Because of weak modulation, the assignment of a unit super-cell in Fig. 4(a) is not as easy as in Fig. 3(d). The region inside the dashed white square in Fig. 4(a) looks like an array of rods over an array of rods rotated by 90 degrees while the region inside the dashed blue square looks like dots for the joints of rods in two layers. Dual lattice feature is clearly observed in Fig. 4(a): the size of dots becomes smaller along the dashed yellow arrow and the dashed white arrow that is in opposite direction to the yellow one; additionally, the yellow and white arrows are shifted by a half of small period. The experimental observation agrees with the simulation in Fig. 4(c) with a dual lattice structure that has been observed in 2D GPSC [26,34].

Fig. 4(d) shows the laser diffraction pattern of 532 nm from the type-3 3D GPSC which is similar to that in type-2 3D GPSC. Diffraction zones in the diffraction pattern are aligned along the parabolic dashed red and yellow lines due to the tilting caused by the four inner interfering beams. The diffraction zone inside the dashed white square has a

low filling fraction but more uniform intensity due to a lower gradient in the unit supercell than that in type-2 GPSC.

Diffraction efficiency is measured for the diffraction zone orders of (0,0), (1,0), (2,0), (1,1), (2,1) and (2,2) in Fig. 4(d). These diffraction zone orders of (0,0), (2,0), and (2,2) are labelled in the figure. From these efficiency numbers, we can tell that most of light are distributed among non-zero orders. For example, 24% of light is distributed in $(\pm 1,0)$ and $(0,\pm 1)$ orders, comparing with 9.9% for (0,0) order.

Table 1. Measured diffraction efficiency for some of diffraction zone orders in Fig. 4(d).

Diffraction zone order	(0,0)	(1,0)	(2,0)	(1,1)	(2,1)	(2,2)
Diffraction efficiency (%)	9.9	6.0	4.8	3.7	2.8	2.6

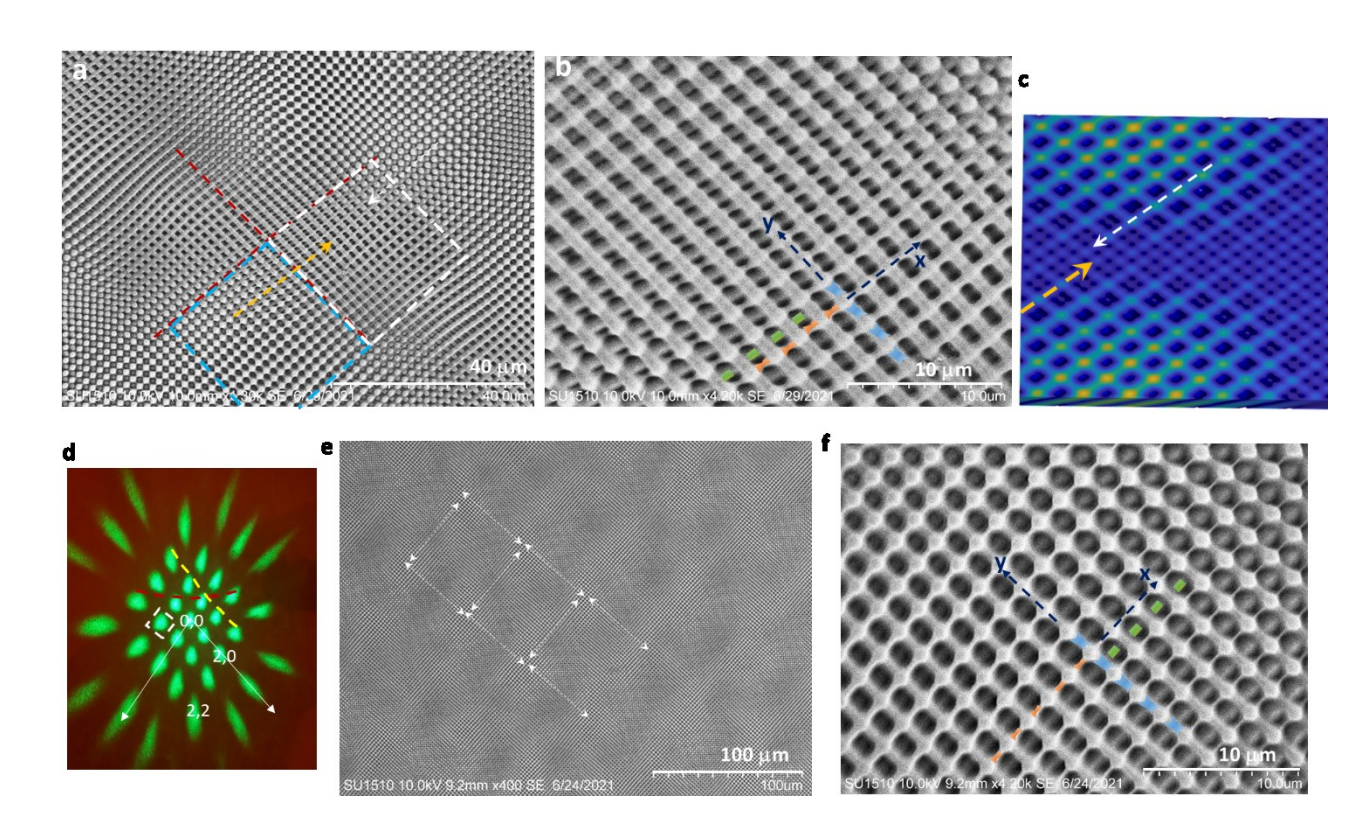


Figure 4. (a) SEM image of type-3 GPSC. The dashed white and blue squares indicate sub-units with more woodpile-like structures and dot-like structures, respectively. The size of the dots decreases along the dashed yellow and white lines. (b) An enlarged view of SEM of type-3 GPSC. (c) Simulation of GPSC shows a decrease in dot sizes along the dashed yellow and white lines. (d) 5x5 diffraction zones from type-3 3D GPSC showing the diffraction orders. (e) SEM image of type-3 3D GPSC that shows the same diffraction zones. (f) Enlarged view of SEM image showing layer-by-layer structure as indicated by dashed orange, blue and green lines.

4. Discussion

The metal deposition on the sample for SEM usually destroys the sample for other purposes therefore we have been using these features in the diffraction zone to distinguish types of 3D GPSCs quickly. These features have been consistently observed, for example, in Fig. 4(e) from a sample that is fabricated on a different day for type-3 3D GPSC. The white arrows indicate the repeatability of patterns with a higher filling fraction of air in DPHPA GPSC than other regions. Layer-by-layer structures are visible in both Fig. 4(b) and 4(f) where dashed orange lines in x-axis indicate the top layer, dashed blue lines in y-axis are for the second layer and dashed green lines are for the third layer that is shifted by a half of lattice period.

DPHPA mixture is a good polymer for a quick proof of concept of holographic structures. However, it is in a liquid form, has a thin film, and is polymerized during the exposure which makes it suboptimal for 3D structures. SU-8 should be used for 3D structure in future work because it is in a solid form and polymerized during post-exposure heating [21,38,39], and a good template for an inversion to silicon materials [40]. With a thick sample in SU-8, it will be interesting to observe the diffraction pattern from different direction as one research group did for super-crystals with complex macroscopic properties in composite ferroelectrics [41].

The study of 3D GPSC is still in its infancy. It can lead toward many potential applications because of the tunability of holographic patterns by phase, intensity and polarization of interfering beams. 3D holographic structure has been studied for their topological properties [42]. Once the interference pattern is inversed to a silicon structure (dielectric constant = 11.9) using the following step functions: $\varepsilon(r) = 1$ when I< Ith; $\varepsilon(r) = 11.9$ when I> Ith [38], we can do simulations of photonic band structure to search for multiple photonic band-gaps and flat bands or electro-magnetic simulation for diffraction patterns and focusing properties [37]. For the light coupling into the 3D GPSC, the type-2 GPSC can couple the light from 360° azimuthal angles and broad zenith angles with less angle gap than the type-3 GPSC while type-3 GPSC can couple light more uniformly than the type-2 one.

So far, we have used four inner beams at $(\pm 1,\pm 1)$ for the nine-beam interference. Further study can include other four beams at $(\pm 1,0)$ and $(0,\pm 1)$ in the nine-beam interference. In such a case, the long-period structure will be rotated by 45 degrees.

5. Conclusions

We have fabricated 3D GPSCs in DPHPA from nine-beam (4 inner, 4 outer beams and 1 central beam arranged in a cone geometry) interference lithography using integrated system of SLM, 4f imaging system and single ROE. We have designed three-types of 3D GPSCs through the engineering of phase pattern in SLM by considering the diffraction efficiency, relative phase shift among the diffracted beams and modulation of phase pattern for the generation of gradient unit super-cell. We have observed diffraction zones instead of diffraction spots due to the fractional diffraction from the unit super-cell. We have observed 3×3 diffraction zones from 3D GPSCs with a weak modulation from inner beams, 5×5 non-uniform diffraction zones from these with a strong gradient unit super-cell, and 5×5 uniform diffraction zones from those with a medium gradient unit super-cell. Moiré PhCs appear in the holographic structure with a strong modulation. These diffraction patterns have been used to characterize 3D GPSCs.

Author Contributions: Conceptualization, Y.L. and J.C.; methodology, Y.L., N.H., S.K, K.A. and J.C; software, N.H., K.A., and S.K.; investigation, U.P., Y.L., N.H. and S.K.; formal analysis, Y.L. and N.H.; writing—original draft preparation, N.H. and Y.L.; writing—review and editing, N.H.; funding acquisition, J.C. and Y.L. All authors have read and agreed to the published version of the manuscript.

Funding: This research was partially supported by the U.S. National Science Foundation, grant numbers 1661842 and 2128367.

Conflicts of Interest: The authors declare no conflict of interest. The funders had no role in the design of the study; in the collection, analyses, or interpretation of data; in the writing of the manuscript, or in the decision to publish the results.

Data Availability Statement: Data will be available upon request.

References

1. John, S. Strong Localization of Photons in Certain Disordered Dielectric Superlattices. *Physical Review Letters* **1987**, 58, 2486-2489. doi:10.1103/PhysRevLett.58.2486.

277
ss 278
e- 279
es 280

- 2. Akahane, Y.; Asano, T.; Song, B.S.; Noda, S. High-Q Photonic Nanocavity in a Two-Dimensional Photonic Crystal. *Nature* **2003**, 425, 944-947. doi:10.1038/nature02063.
- 3. Tandaechanurat, A.; Ishida, S.; Guimard, D.; Nomura, M.; Iwamoto, S.; Arakawa, Y. Lasing Oscillation in a Three-Dimensional Photonic Crystal Nanocavity with a Complete Bandgap. *Nature Photonics* **2011**, *5*, 91-94. Doi:10.1038/nphoton.2010.286.
- 4. Delgoffe, A.; Miranda, A.; Rigal, B.; Lyasota, A.; Rudra, A.; Dwir, B.; Kapon, E. Tilted-Potential Photonic Crystal Cavities for Integrated Quantum Photonics. *Optics Express* **2019**, 27, 21822-21833. doi:10.1364/oe.27.021822.
- 5. Perczel, J.; Borregaard, J.; Chang, D.E.; Yelin, S.F.; Lukin, M.D. Topological Quantum Optics Using Atomlike Emitter Arrays Coupled to Photonic Crystals. *Physical Review Letters* **2020**, 124, 83603-83610. doi:10.1103/PhysRevLett.124.083603.
- 6. Kim, S.; Fröch, J.E.; Christian, J.; Straw, M.; Bishop, J.; Totonjian, D.; Watanabe, K.; Taniguchi, T.; Toth, M.; Aharonovich, I. Photonic Crystal Cavities from Hexagonal Boron Nitride. *Nature Communications* **2018**, *9*,1-8. doi:10.1038/s41467-018-05117-4.
- 7. Bhattacharya, S.; Baydoun, I.; Lin, M.; John, S. Towards 30% Power Conversion Efficiency in Thin-Silicon Photonic-Crystal Solar Cells. *Physical Review Applied* **2019**, *11*, 14005-14031. doi:10.1103/PhysRevApplied.11.014005.
- 8. Liu, W.; Ma, H.; Walsh, A. Advance in Photonic Crystal Solar Cells. *Renewable and Sustainable Energy Reviews* 2019, 116. 1-19.
- 9. Hassan, S.; Alnasser, K.; Lowell, D.; Lin, Y. Effects of Photonic Band Structure and Unit Super-Cell Size in Graded Photonic Super-Crystal on Broadband Light Absorption in Silicon. *Photonics* **2019**, *6*, 50-58. doi:10.3390/photonics6020050.
- 10. Maho, A.; Lobet, M.; Daem, N.; Piron, P.; Spronck, G.; Loicq, J.; Cloots, R.; Colson, P.; Henrist, C.; Dewalque, J. Photonic Structuration of Hybrid Inverse-Opal TiO2- Perovskite Layers for Enhanced Light Absorption in Solar Cells. *ACS Applied Energy Materials* **2021**, *4*, 1108-1119. doi:10.1021/acsaem.0c02124.
- 11. Lobet, M.; Piron, P.; Dewalque, J.; Maho, A.; Deparis, O.; Henrist, C.; Loicq, J. Efficiency Enhancement of Perovskite Solar Cells Based on Opal-like Photonic Crystals. *Optics Express* **2019**, 27, 32308-32322. Doi:10.1364/oe.27.032308.
- 12. Hwang, D.K.; Lee, B.; Kim, D.H. Efficiency Enhancement in Solid Dye-Sensitized Solar Cell by Three-Dimensional Photonic Crystal. *RSC Advances* **2013**, *3*, 3017-3023. doi:10.1039/c2ra22746k.
- 13. Kim, Y.D.; Han, K.-H.; Park, S.-J.; Kim, J.-B.; Shin, J.-H.; Kim, J.J.; Lee, H. Enhanced Light Extraction Efficiency in Organic Light Emitting Diodes Using a Tetragonal Photonic Crystal with Hydrogen Silsesquioxane. *Optics Letters* **2014**, *39*, 5901-5904. doi:10.1364/ol.39.005901.
- 14. Ishihara, K.; Fujita, M.; Matsubara, I.; Asano, T.; Noda, S.; Ohata, H.; Hirasawa, A.; Nakada, H.; Shimoji, N. Organic Light-Emitting Diodes with Photonic Crystals on Glass Substrate Fabricated by Nanoimprint Lithography. *Applied Physics Letters* **2007**, *90*, 111114. Doi:10.1063/1.2713237.
- Zhang, Y.; Biswas, R. High Light Outcoupling Efficiency from Periodically Corrugated OLEDs. ACS Omega 2021,
 6, 9291-9301. doi:10.1021/acsomega.1c00903.
- Hassan, S.; Lowell, D.; Lin, Y. High Light Extraction Efficiency into Glass Substrate in Organic Light-Emitting
 Diodes by Patterning the Cathode in Graded Superlattice with Dual Periodicity and Dual Basis. *Journal of Applied Physics* 2017, 121, 233104. doi:10.1063/1.4986233.

- 17. Alnasser, K.; Hassan, S.; Kamau, S.; Zhang, H.; Lin, Y. Enhanced Light Extraction from Organic Light-Emitting Diodes by Reducing Plasmonic Loss through Graded Photonic Super-Crystals. *Journal of the Optical Society of America B* **2020**, *37*, 1283-1289. Doi:10.1364/josab.387780.
- 18. Ning, H.; Pikul, J.H.; Zhang, R.; Li, X.; Xu, S.; Wang, J.; Rogers, J.A.; King, W.P.; Braun, P. v. Holographic Patterning of High-Performance on-Chip 3D Lithium-Ion Microbatteries. *Proc Natl Acad Sci U S A* **2015**, *112* 6573-6578. doi:10.1073/pnas.1423889112.
- 19. Kamali, S.M.; Arbabi, E.; Kwon, H.; Faraon, A. Metasurface-Generated Complex 3-Dimensional Optical Fields for Interference Lithography. *Proc Natl Acad Sci U S A* **2019**, *116*, 21379-21384. Doi:10.1073/pnas.1908382116.
- 20. Jeon, T.; Kim, D.H.; Park, S.G. Holographic Fabrication of 3D Nanostructures. *Advanced Materials Interfaces* 2018, 5, 1800330. doi:10.1002/admi.201800330
- 21. Lin, Y.; Herman, P.R.; Darmawikarta, K. Design and Holographic Fabrication of Tetragonal and Cubic Photonic Crystals with Phase Mask: Toward the Mass-Production of Three-Dimensional Photonic Crystals. *Applied Physics Letters* **2005**, *86*, 071117. doi:10.1063/1.1865329.
- 22. Park, H.; Lee, S. Double Gyroids for Frequency-Isolated Weyl Points in the Visible Regime and Interference Lithographic Design. *ACS Photonics* **2020**, *7*, 1577-1585. Doi:10.1021/acsphotonics.0c00532.
- 23. Sun, X.; Wu, F.; Wang, S.; Qi, Y.; Zeng, Y. Design of Gradient Photonic Crystal Lens Array Using Two-Parameter Hexagonal Prism Interferometer. *Guangxue Xuebao/Acta Optica Sinica* **2020**, 40, 0222002. Doi:10.3788/AOS202040.0222002.
- 24. Behera, S.; Joseph, J. Single-Step Optical Realization of Bio-Inspired Dual-Periodic Motheye and Gradient-Index-Array Photonic Structures. *Optics Letters* **2016**, *41*, 3579-3582. doi:10.1364/ol.41.003579.
- 25. Lowell, D.; Hassan, S.; Sale, O.; Adewole, M.; Hurley, N.; Philipose, U.; Chen, B.; Lin, Y. Holographic Fabrication of Graded Photonic Super-Quasi-Crystals with Multiple-Level Gradients. *Applied Optics* **2018**, *57*,6598-6604. doi:10.1364/ao.57.006598.
- 26. Hassan, S.; Sale, O.; Lowell, D.; Hurley, N.; Lin, Y. Holographic Fabrication and Optical Property of Graded Photonic Super-Crystals with a Rectangular Unit Super-Cell. *Photonics* **2018**, *5*, 34-44. doi:10.3390/photonics5040034.
- 27. Lowell, D.; Hassan, S.; Adewole, M.; Philipose, U.; Chen, B.; Lin, Y. Holographic Fabrication of Graded Photonic Super-Crystals Using an Integrated Spatial Light Modulator and Reflective Optical Element Laser Projection System. *Applied Optics* **2017**, *56*,9888-9891. doi:10.1364/ao.56.009888.
- 28. Sale, O.; Hassan, S.; Hurley, N.; Alnasser, K.; Philipose, U.; Zhang, H.; Lin, Y. Holographic Fabrication of Octagon Graded Photonic Supercrystal and Potential Applications in Topological Photonics. *Frontiers of Optoelectronics* **2020**, *13*, 12-17. doi:10.1007/s12200-019-0941-2.
- 29. Oudich, M.; Su, G.; Deng, Y.; Benalcazar, W.; Huang, R.; Gerard, N.J.R.K.; Lu, M.; Zhan, P.; Jing, Y. Photonic Analog of Bilayer Graphene. *Physical Review B* **2021**, *103*,214311-214321. Doi:10.1103/PhysRevB.103.214311.
- 30. Lou, B.; Zhao, N.; Minkov, M.; Guo, C.; Orenstein, M.; Fan, S. Theory for Twisted Bilayer Photonic Crystal Slabs. *Physical Review Letters* **2021**, *126*,136101-136107. doi:10.1103/PhysRevLett.126.136101.
- Dong, K.; Zhang, T.; Li, J.; Wang, Q.; Yang, F.; Rho, Y.; Wang, D.; Grigoropoulos, C.P.; Wu, J.; Yao, J. Flat Bands in Magic-Angle Bilayer Photonic Crystals at Small Twists. *Physical Review Letters* **2021**, *126*,223601-223607. doi:10.1103/PhysRevLett.126.223601.
- 32. Alnasser, K.; Kamau, S.; Hurley, N.; Cui, J.; Lin, Y. Photonic Band Gaps and Resonance Modes in 2d Twisted Moiré Photonic Crystal. *Photonics* **2021**, *8*, 408-418. doi:10.3390/photonics8100408.

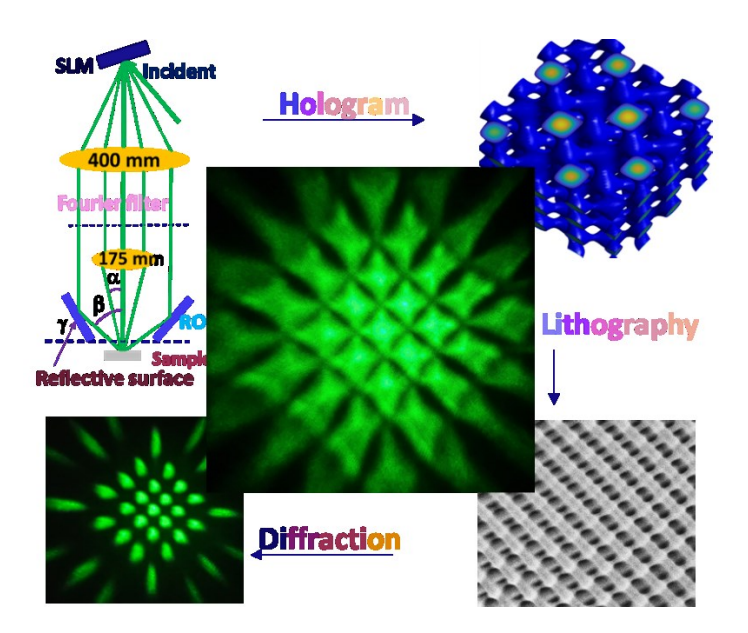
- 33. Alnasser, K.; Kamau, S.; Hurley, N.; Cui, J.; Lin, Y. Resonance Modes in Moiré Photonic Patterns for Twistoptics. *OSA Continuum* **2021**, *4*, 1339-1347. doi:10.1364/osac.420912.
- 34. Lowell, D.; Lutkenhaus, J.; George, D.; Philipose, U.; Chen, B.; Lin, Y. Simultaneous Direct Holographic Fabrication of Photonic Cavity and Graded Photonic Lattice with Dual Periodicity, Dual Basis, and Dual Symmetry. *Optics Express* **2017**, *25*, 14444-14452. Doi:10.1364/oe.25.014444.
- 35. Ohlinger, K.; Lutkenhaus, J.; Arigong, B.; Zhang, H.; Lin, Y. Spatially Addressable Design of Gradient Index Structures through Spatial Light Modulator Based Holographic Lithography. *Journal of Applied Physics* **2013**, 114, 23102. Doi:10.1063/1.4837635.
- 36. Case, W.B.; Tomandl, M.; Deachapunya, S.; Arndt, M. Realization of Optical Carpets in the Talbot and Talbot-Lau Configurations. *Optics Express* **2009**, *17*, 20966-20974. doi:10.1364/oe.17.020966.
- Hassan, S.; Jiang, Y.; Alnasser, K.; Hurley, N.; Zhang, H.; Philipose, U.; Lin, Y. Generation of over 1000 Diffraction Spots from 2D Graded Photonic Super-Crystals. *Photonics* **2020**, 7, 27. https://doi.org/10.3390/photonics7020027.
- Lowell, D.; George, D.; Lutkenhaus, J.; Tian, C.; Adewole, M.; Philipose, U.; Zhang, H.; Lin, Y. Flexible Holographic Fabrication of 3D Photonic Crystal Templates with Polarization Control through a 3D Printed Reflective Optical Element. *Micromachines* **2016**, *7*, 128. doi:10.3390/mi7070128.
- George, D.; Lutkenhaus, J.; Lowell, D.; Moazzezi, M.; Adewole, M.; Philipose, U.; Zhang, H.; Poole, Z.L.; Chen, K.P.; Lin, Y. Holographic Fabrication of 3D Photonic Crystals through Interference of Multi-Beams with 4 + 1, 5 + 1 and 6 + 1 Configurations. *Optics Express* **2014**, *22*, 22421. doi:10.1364/oe.22.022421.
- Tétreault, N.; von Freymann, G.; Deubel, M.; Hermatschweiler, M.; Pérez-Willard, F.; John, S.; Wegener, M.; Ozin, G.A. New Route to Three-Dimensional Photonic Bandgap Materials: Silicon Double Inversion of Polymer Templates. *Advanced Materials* **2006**, *18*, 457. doi:10.1002/adma.200501674.
- 41 Pierangeli, D.; Ferraro, M.; di Mei, F.; di Domenico, G.; de Oliveira, C.E.M.; Agranat, A.J.; DelRe, E. Super-Crystals in Composite Ferroelectrics. *Nature Communications* **2016**, *7*, **10674**. doi:10.1038/ncomms10674.
- Park, H.; Lee, S. Double Gyroids for Frequency-Isolated Weyl Points in the Visible Regime and Interference Lithographic Design. *ACS Photonics* **2020**, *7*, 1577. doi:10.1021/acsphotonics.0c00532.

Cover page information

1. A short introduction of your paper with up to 800 characters *including the spaces and punctuation*.

The laser diffraction from periodic structures usually shows isolated and sharp point-pattern at zeroth and higher orders. Here, we report large-area diffraction zones in the holographic three-dimensional graded photonic super-crystals that can be classified as twisted photonic crystals. They also appear as moiré photonic crystals when there is a strong modulation. The diffraction spots due to the fractional orders are merged into diffraction zones. These diffraction-zone patterns not only demonstrate a characterization method for the fabricated twisted photonic crystals but also prove their unique optical properties of the coupling of light from zones with 360° azimuthal angles and broad zenith angles.

2. A high-resolution picture with no copyright restrictions.



3. A shorter title of your paper with up to 80 characters *including the spaces and punctuation*.

Laser Diffraction Zones and Spots from Gradient and Moiré Photonic Crystals

- 440 a 441 - 442 t 443